International Journal of Fracture (2005) 133:197–222
DOI 10.1007/s10704-005-3122-9

Boundary element method for *J*-integral and stress intensity factor computations in three-dimensional interface cracks

JHONNY E. ORTIZ[1] and ADRIÁN P. CISILINO[2,*]
[1] *Department of Mechanical Engineering, Universidad Nacional de Trujillo, Trujillo, Perú*
[2] *Department of Mechanical Engineering, Welding and Fracture Division, INTEMA CONICET, Universidad Nacional de Mar del Plata, Av. Juan B. Justo 4302, (7600) Mar del Plata, Argentina*
[*] *Author for correspondence (E-mail: cisilino@fi.mdp.edu.ar)*

Received 22 January 2004; accepted in revised form 3 March 2005

Abstract. A general numerical tool for the analysis of three-dimensional bimaterial interface cracks is presented in this paper. The proposed tool is based on a multidomain formulation of the Boundary Element Method (BEM), with the crack located at the interface of the domain. Mixed mode stress intensity factors are computed along the three-dimensional crack fronts using the Energy Domain Integral (EDI) methodology and decoupled via the Interaction Integral. The capability of the procedure is demonstrated by solving a number of examples. The last of these examples consists in a thick centre cracked panel for which the behaviour of the *J*-integral and the mixed-mode stress intensity factors along the crack front is studied as a function of the material mismatch.

Key words: Energy domain integral, interfacial fracture mechanics, interaction integral, three-dimensional interface cracks.

1. Introduction

The overall mechanical properties of composite materials depend heavily on the nature of the bond at bimaterial interfaces. Unfortunately, interfacial delamination and fracture are commonly observed problems that may ultimately limit the use of these materials, which range from ceramic and metal matrix composites for the aerospace industry to nanoscale structures for microelectronics applications. The need to improve the fracture toughness of composite materials has led to significantly progress in the area of interfacial fracture mechanics. During the past few decades, comprehensive analyses have been carried out, and many questions regarding the mechanic of interface fracture have been answered. However, progress has been generally mainly focused in the two-dimensional idealization of an interface crack, and limited work has been conducted on the three-dimensional aspects of interface fracture. This is in part due to the extreme complexity of such problems and the very large computational efforts required for their numerical analysis. However, given the material mismatch at the interface boundary, it is expected that the three-dimensional effects play a more significant role in flawed bimaterial structures than in their homogenous counterparts.

The BEM has been extensively employed to analyse a variety of problems involving two- and three-dimensional interface cracks. Among others, two-dimensional

BEM analysis are reported by Cho et al. (1992), who analysed the problem of interface cracks in dissimilar anisotropic materials; Yuuki and Xu (1994), who evaluated the effect of residual stresses; Sladeck and Sladeck (1997), who conducted a study on T-stresses; Kwon and Dutton (1991), who tackled the problem of cracks in the direction normal to the bimaterial interface; and Selcuk et al. (1994) and Beer (1993), who used BEM for the prediction of interfacial crack propagation. Likewise, París et al. (1996) and Varna et al. (1997) studied the effect of crack-face contact on the fibre/matrix debonding, while Liu and Xu (2000) considered the effect of the fibre coating on the debonding process. Three dimensional analyses can be found in the papers by Raveendra and Banerjee (1991) and Wen and Aliabadi (1999). While in the former stress intensity factors are computed using displacement results, the later also explores methods based on stress results and energy principles.

Although many authors propose displacement and stress extrapolation methods to determine stress intensity factors from BEM results (see for example Yuuki and Cho, 1989; Tan and Gao, 1990; Raveendra and Banerjee, 1991; He et al., 1994; Mao and Sun, 1995; Wen and Aliabadi, 1999) *J*-integral methods constitute a more robust approach. Note that BEM is specially suited for the evaluation of path independent integrals, since the required stresses, strains and derivatives of displacements at internal points can be directly obtained from their boundary integral representations. It also has been shown that BEM produces more accurate stresses and strains at internal points when compared with other numerical techniques, and therefore better results can be achieved. Application of the *J*-integral methodology for two-dimensional interface cracks can be found in the works by Miyazaki et al. (1993) and de Paula and Aliabadi (1997).

The *J*-integral as devised by Rice (1968) characterizes the crack driving force for two-dimensional problems, therefore, for general three-dimensional cases involving cracks of arbitrary shape an alternative form for the *J*-integral is needed. Three basic schemes have evolved for the numerical computation of the *J*-integral in three dimensions: virtual crack extension methods (Park, 1974; Hellen, 1975) generalization of Rice's contour integral (Carpenter et al., 1986), and domain integral methods (Moran and Shih, 1987; Nikishkov and Atluri 1987; Saliva et al., 2000). Among the available schemes for the numerical computation of the *J*-integral in three dimensions, the Energy Domain Integral (EDI) due to Moran and Shih (1987) is employed in this work. Previous work by one of the authors of this paper has proved the versatility and efficiency of the EDI in the three-dimensional BEM analysis of isotropic cracked bodies (Cisilino et al., 1998; Cisilino and Aliabadi, 1999). Together with the EDI the interaction or M_1-integral methodology due to Chen and Shield (1997) is employed for decoupling the *J*-integral into the mixed-mode stress intensity factors. The M_1-integral methodology has been recently reported in a number of papers using FEM to compute stress intensity factors along three-dimensional interface cracks (see Gosz, Dolbow and Moran 1998; Nagashima; Omoto and Tani, 2003). Using BEM, the M_1-integral methodology has been only implemented for two-dimensional interface problems by Miyazaki et al. (1993) and by Cisilino and Ortiz for three dimensional homogenous bodies (Cisilino and Ortiz, 2004).

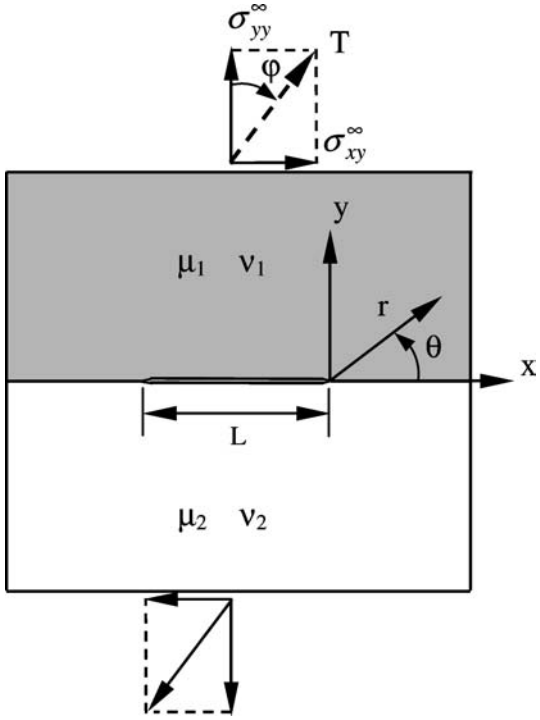

Figure 1. Schematic representation of bimaterial plate with an interface crack: coordinate system in the region of the crack tip and remote tension and shear loading.

2. Crack tip field and bimaterial interfaces

2.1. Singular stress field

Consider the plane problem of an open interface crack between two dissimilar isotropic materials as shown in Figure 1. For convenience, we adopt a local polar coordinate system centred at the crack tip, and we label the material occupying the upper half-plane as material 1 with Young modulus E_1 and Poisson ratio ν_1. The material occupying the lower half-plane has Young modulus E_2 and Poisson ratio ν_2. The stress field very close to the crack front corresponds to the asymptotic field based on the two-dimensional solutions due to Williams (1959). The form of the bimaterial stress field given by Rice et al. (1990) (with the addition of Mode III) is

$$\sigma_{ij} = \frac{1}{\sqrt{2\pi r}} \left\{ \mathrm{Re}\left[\mathbf{K} r^{i\varepsilon}\right] \tilde{\sigma}^{\mathrm{I}}_{ij}(\theta, \varepsilon) + \mathrm{Im}\left[\mathbf{K} r^{i\varepsilon}\right] \tilde{\sigma}^{\mathrm{II}}_{ij}(\theta, \varepsilon) + K_{\mathrm{III}} \tilde{\sigma}^{\mathrm{III}}_{ij}(\theta) \right\}, \tag{1}$$

where r and θ are the in-plane coordinates of the plane normal to the crack front (see Figure 1), $\mathbf{K}$ is defined as the complex stress intensity factor for the in-plane modes, $\mathbf{K} = K_{\mathrm{I}} + i K_{\mathrm{II}}$, and $\tilde{\sigma}_{ij}$ are the angular variations of stress components for each mode (The explicit form of the asymptotic stress and displacement components are given in Appendix A). The oscillatory index ε is:

$$\varepsilon = \frac{1}{2\pi} \ln\left[\frac{\kappa_1 \mu_2 + \mu_1}{\kappa_2 \mu_1 + \mu_2}\right] = \frac{1}{2\pi} \ln\left[\frac{1-\beta}{1+\beta}\right]. \tag{2}$$

Here, $\kappa_j = 3 - 4\nu_j$ for plane strain and $\kappa_j = (3 - \nu_j)/(1 + \nu_j)$ for plane stress, $\mu_j = E_j/2(1 + \nu_j)$ is the shear modulus, and the subscripts $j = 1,\ 2$ refer to the materials above and below the crack plane, respectively. Furthermore, β is one of Dundurs' parameters. In two-dimensional problems, the solution can be characterized by the two Dundurs' parameters, and they are defined as Dundurs (1969):

$$\alpha = \frac{\mu_1(\kappa_2 + 1) - \mu_2(\kappa_1 + 1)}{\mu_2(\kappa_1 + 1) + \mu_1(\kappa_2 + 1)}, \qquad \beta = \frac{\mu_1(\kappa_2 - 1) - \mu_2(\kappa_1 - 1)}{\mu_2(\kappa_1 + 1) + \mu_1(\kappa_2 + 1)}. \tag{3}$$

Unlike the two-dimensional cases, the above parameters are not sufficient to characterize the full-field deformation of three dimensional boundary value problems. Note that a bimaterial combination yields different Dundurs' parameters under plain-strain and plane-stress conditions.

2.2. Near tip contact zone

Comninou (1977) showed that the solutions for the interface crack must allow for a contact zone at the crack tips. Thus, linear elastic fracture mechanics procedures (i.e. characterizing crack growth in terms of $K_{\mathrm{I}} + iK_{\mathrm{II}}$) are valid when the inevitable nonlinear contact zone at the crack tip is sufficiently small (Rice, 1988). An elementary estimation of the contact zone size, assuming that it is small compared to crack size, is given by finding the largest distance r_{c} from the crack tip for which the opening gap between the crack faces vanishes. Assuming that $\varepsilon > 0$ (if not we can just exchange the labels "1" and "2") and based on the displacement asymptotic fields due to Williams (1959) and Rice (1988) proposed the following expression for computing r_{c}:

$$r_{\mathrm{c}} = L \exp[-(\varphi + \pi/2)/\varepsilon], \tag{4}$$

where L stands for the crack length and φ gives the direction of the remote traction vector as illustrated in Figure 1. An interesting checking of the adequacy of this estimation can be found in Paris et al. (1996), showing that contact zone is smaller than the interpenetration zone.

In general, ε increases with the increase of stiffness ratio, μ_1/μ_2. For example, if we take the material combination given by cork (with $\nu \approx 0$) and alumina (Al_2O_3) so that $\mu_1/\mu_2 \approx 0$, then ε yields its largest feasible value (at least for solids with $\nu \geqslant 0$), namely, $\varepsilon = 0.175$. Representative values of ε are considerably lower for various combinations of interest for practical metal and nonmetal interfaces. For example Hutchinson et al. (1987) give $\varepsilon = 0.039$ for Ti/Al_2O_3, $\varepsilon = 0.028$ for Cu/Al_2O_3, $\varepsilon = 0.019$ for Nb/Al_2O_3, $\varepsilon = 0.011$ for Si/Cu, $\varepsilon = 0.005$ for MgO/Ni, and $\varepsilon = 0.004$ for Au/MgO based on elastic parameters that they tabulated.

If one adopts $r_{\mathrm{c}}/L < 0.01$ as a suitable restriction on r_{c} so that the small scale contact zone concept may be applied, that is, the field may be regarded as being characterized by the complex $\mathbf{K}$, then one requires $\varphi > -\pi/2 + 4.605\varepsilon$ (Rice, 1988). Thus, is required for validity of the linear elastic fracture mechanics approach outlined above that $\varphi > -50^\circ$ when $\varepsilon = 0.15, \varphi > -77^\circ$ when $\varepsilon = 0.05$, and $\varphi > -87^\circ$ when $\varepsilon = 0.01$. These restrictions will generally be met in practical cases for which there are some nonnegligible tensile component of the loading relative to the crack (Hutchinson et al., 1987).

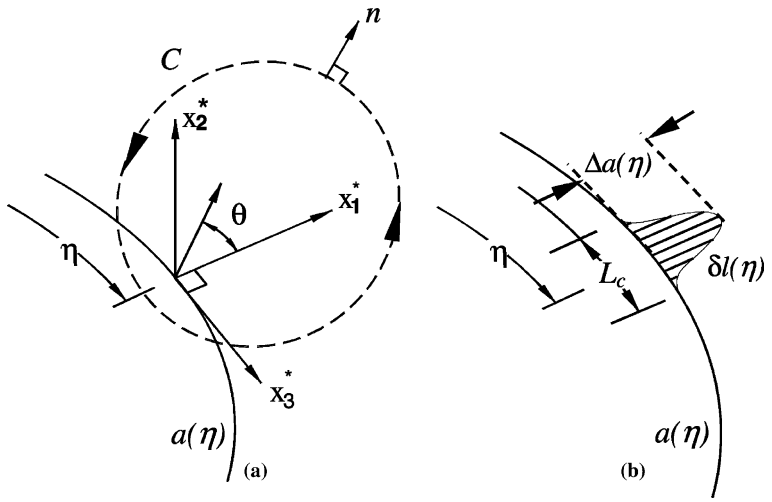

Figure 2. (a) Definition of the local orthogonal Cartesian coordinates at point η on the crack front, (b) Virtual crack front advance.

2.3. Three-dimensional energy release rate

Based on energy arguments, the relationship between the energy release rate G (or the equivalent J-integral in the case of an elastic medium) and the stress intensity factors of an interface crack is Nakamura (1991):

$$G = \frac{1}{E^* \cosh^2(\pi\varepsilon)} \left[K_{\mathrm{I}}^2 + K_{\mathrm{II}}^2\right] + \frac{1}{2\mu^*} K_{\mathrm{III}}^2. \tag{5}$$

Here, E^* and μ^* are the average/effective plane-strain tensile modulus and shear modulus of the two materials, respectively, and they are:

$$\frac{1}{E^*} = \frac{1}{2}\left(\frac{1-\nu_1^2}{E_1} + \frac{1-\nu_2^2}{E_2}\right), \quad \frac{1}{\mu^*} = \frac{1}{2}\left(\frac{1}{\mu_1} + \frac{1}{\mu_2}\right). \tag{6}$$

3. *J*-integral and stress intensity factor computation

3.1. The energy domain integral

Consider a three-dimensional crack front with a continuously turning tangent as depicted in Figure 2a. Define a local coordinate system x^* at position η, where the crack energy release rate is evaluated, given by x_1^* normal to the crack front, x_2^* normal to the crack plane, and x_3^* tangent to the crack front.

Following Natha and Moran (1993), the general crack-tip contour integral along three-dimensional crack front takes the form (see Figure 2)

$$I(\eta) = \lim_{C \to 0} \delta l(\eta) \int_{C(\eta)} \left(w\delta_{kj} - \sigma_{ij}^* u_{i,k}^*\right) n_j \mathrm{d}C, \tag{7}$$

where w is the strain energy density, σ_{ij}^* and $u_{i,1}^*$ are Cartesian components of stress and displacement derivatives expressed in the local system x^*, $\delta l(\eta)$ is the local crack

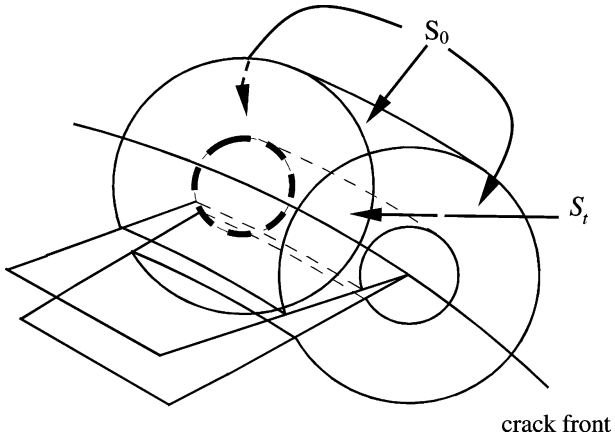

Figure 3. Tubular domain surrounding a segment of the crack front.

extension, n_j is the unit vector normal to the contour C (which lies in the $x_1^* - x_2^*$ plane) and $\mathrm{d}C(\eta)$ is the differential of the arc length C (see Figure 2a). It is worth noting that, although Equation (7) comes from a two-dimensional analysis, it applies for the three-dimensional case, as in the limit as $C \to 0$, plain strain conditions prevail so that three-dimensional fields approach the plane problem.

In order to derive the equivalent domain representation of Equation (7), we consider a small segment L_c of the crack front that lies in the local $x_1^* - x_3^*$ plane as shown in Figure 2(b). Next we assume that the segment undergoes a virtual crack advance in the plane of the crack, and we define the magnitude of the advance at each point η as $\Delta a(\eta)$. We note that $\Delta a(\eta)$ varies continuously along L_c and vanishes at each end of the segment. Now let:

$$\bar{I} = \int_{L_\mathrm{C}} I(\eta)\Delta a(\eta)\mathrm{d}\eta, \tag{8}$$

where $I(\eta)$ is the integral defined in Equation (7). When $I(\eta)$ belongs to the pointwise energy release rate, $\bar{I}$ gives the total energy released when the finite segment L_c undergoes the virtual crack advance.

The appropriate domain form of the pointwise crack-tip contour integral can be obtained from Equation (8) by considering a tubular domain V surrounding the crack segment (see Figure 3). As shown in the figure, the surface S_t is formed by translating the contour C along the segment L_c, and S_o stands for the outer surface of V including the ends. Next an auxiliary function q is introduced, which is sufficiently smooth in V and it is defined on the surfaces of V as follows:

$$q = \begin{cases} \Delta a(\eta) \cdot \delta l(\eta) & \text{on } S_\mathrm{t}, \\ 0 & \text{on } S_\mathrm{o}. \end{cases} \tag{9}$$

Finally, in the limit as the tubular surface S_t is shrunk onto the crack segment L_c, and in the absence of crack face tractions, we obtain the domain integral:

$$\bar{I} = \int_V \left(\sigma_{ij}^* u_{j,k}^* - w\delta_{ki}\right)_{q,i} \mathrm{d}V. \tag{10}$$

In the evaluation of the energy release rate in the absence of body forces the integral given by Equation (10) reduces to the domain representation of the familiar J-integral. A simple relationship between $J(\eta)$ and the point-wise crack-tip integral $I(\eta)$ can be obtained if it is assumed that $I(\eta)$ is constant along the segment L_c. Then, it follows directly from Equation (8) that

$$J(\eta) = \frac{\bar{I}}{\int_{L_c} \Delta a(\eta) \mathrm{d}\eta}. \tag{11}$$

3.2. The interaction integral

In this section, the interaction or M_1-integral methodology for decoupling three-dimensional mixed-mode stress intensity factors is presented. This methodology is based on the principle of superposition. Let us consider two equilibrium states with field variables denoted by the superscripts (1) and (2), respectively. Superposition of the two equilibrium states leads to another one, (1+2), for which the stress intensity factors $K_j^{(1+2)}$ can be written as:

$$K_j^{(1+2)} = K_j^{(1)} + K_j^{(2)} \quad (j = \mathrm{I},\ \mathrm{II},\ \mathrm{III}). \tag{12}$$

The stress intensity factors can be related to the J-integral for the superimposed state (1+2) using Equation (5), what results in:

$$J^{(1+2)} = \frac{1}{E^* \cosh^2(\pi\varepsilon)} \left[\left(K_{\mathrm{I}}^{(1+2)} \right)^2 + \left(K_{\mathrm{II}}^{(1+2)} \right)^2 \right] + \frac{1}{2\mu^*} \left(K_{\mathrm{III}}^{(1+2)} \right)^2, \tag{13}$$

where E^* and μ^* are the effective Young's and shear modulus defined in Section 2, and ε stands for the bimaterial constant defined in Equation (2). Equation (13) can be rewritten in terms of the stress intensity factors for the equilibrium states (1) and (2), to give:

$$J^{(1+2)} = J^{(1)} + J^{(2)} + \frac{2}{E^* \cosh^2(\pi\varepsilon)} \left[K_{\mathrm{I}}^{(1)} K_{\mathrm{I}}^{(2)} + K_{\mathrm{II}}^{(1)} K_{\mathrm{I}}^{(2)} \right] + \frac{1}{\mu^*} K_{\mathrm{III}}^{(1)} K_{\mathrm{III}}^{(2)}. \tag{14}$$

Then, the M_1-integral is defined as:

$$M_1 = J^{(1+2)} - J^{(1)} - J^{(2)} = \frac{2}{E^* \cosh^2(\pi\varepsilon)} \left[K_{\mathrm{I}}^{(1)} K_{\mathrm{I}}^{(2)} + K_{\mathrm{II}}^{(1)} K_{\mathrm{I}}^{(2)} \right] + \frac{1}{\mu^*} K_{\mathrm{III}}^{(1)} K_{\mathrm{III}}^{(2)}. \tag{15}$$

Using Equation(10) a domain representation of the M_1-integral can be obtained as follows:

$$M_1 = \int_V \left(\sigma_{ij}^{*(1)} u_{j,k}^{*(2)} + \sigma_{ij}^{*(2)} u_{j,k}^{*(1)} - \sigma_{ij}^{*(1)} \varepsilon_{ij}^{*(2)} \delta_{ki} \right) q_{,i} \mathrm{d}V. \tag{16}$$

For the decoupling of the mixed-mode stress intensity factors, the problem under consideration is selected as equilibrium state (1), so that the field variables $\sigma_{ij}^{*(1)}$ and $u_{j,k}^{*(1)}$ will be obtained in this work from the results of a boundary element analysis. On the other hand, the plain-strain solutions for the asymptotic crack-tip fields given in Appendix 1 with prescribed stress intensity factors K_{I}, K_{II} and K_{III}, are selected as

equilibrium state (2). The field variables related with the equilibrium state (2), $\sigma_{ij}^{*(2)}$, $u_{j,k}^{*(2)}$ and $\varepsilon_{ij}^{*(2)}$ can be calculated from these asymptotic solutions using basic continuum mechanics relationships. Finally, the M_1-integral defined in Equation (16) can be computed using the field variables related with the equilibrium states (1) and (2). By using three sets of asymptotic solutions, ($K_{\mathrm{I}}^{(2)}=1,\ K_{\mathrm{II}}^{(2)}=0,\ K_{\mathrm{III}}^{(2)}=0$), ($K_{\mathrm{I}}^{(2)}=0,\ K_{\mathrm{II}}^{(2)}=1,\ K_{\mathrm{III}}^{(2)}=0$) and ($K_{\mathrm{I}}^{(2)}=0,\ K_{\mathrm{II}}^{(2)}=0,\ K_{\mathrm{III}}^{(2)}=1$) it is possible to obtain the stress intensity factor solutions for individual modes from Equation (15) as follows:

$$
\begin{aligned}
K_{\mathrm{I}}^{(1)} &= \frac{E^{*}\cosh^{2}(\pi\varepsilon)}{2} M_1^{a},\\
K_{\mathrm{II}}^{(1)} &= \frac{E^{*}\cosh^{2}(\pi\varepsilon)}{2} M_1^{b},\\
K_{\mathrm{III}}^{(1)} &= \frac{E^{*}\cosh^{2}(\pi\varepsilon)}{2} M_1^{c},
\end{aligned}
\tag{17}
$$

where M_1^{a}, M_1^{b} and M_1^{c} are the values of the M_1-integral calculated using the three sets of asymptotic solutions.

It is important to point out two limitations for the present implementation of the M_1-integral. The first one is related with the shape of the crack front. The above procedure is only valid for straight crack fronts, since the application of the M_1-integral to curved crack fronts requires the inclusion of extra terms in Equation (16) (Gosz et al., 1998). The second limitation concerns to the validity of the M_1-integral in the region near the terminal point of the interface crack at a free surface. It turns out that the three-dimensional singularity field near the terminal point of the interface crack at the free surface is more singular than $1/\sqrt{r}$ singularity of the interior fields. For a wide selection of material pairs, reported results show that the eigenvalue of the dominant singularity, $\mathrm{O}(r^{-s})$, is real and s increases from 0.5 to 0.75 as the moduli mismatch increases (Bazant and Estenssorrow, 1979; Barsoum and Chen, 1991; Ghahremani and Shih, 1992). Since the M_1 integral is based upon the assumption that the near-crack tip fields are asymptotic to the plane strain fields (see Section 2), the above introduced procedure is not applicable at the intersection of the crack front with a free surface. Please also note that the loss of dominance of the $1/\sqrt{r}$ singularity at the free surface is also a limitation for the applicability of the J-integral.

4. Boundary element analysis

The computation of the J-integral and stress intensity factors via the M_1-integral methodology were implemented in the BEM code as a post-processing procedure, and so it could be applied to the results from a particular model at a later stage. In order to account for the different material properties at both sides of the crack, a multiple domain BEM formulation was used (see Figure 4). The BEM formulation follows standard procedures, for which the equilibrium and continuity conditions are enforced at the common interface between the domains (Brebbia et al., 1984).

Most of the problems analyzed in this work possess symmetry in their geometric configurations and material properties. For such cases, conventionally, only the symmetric portion of the domain is analysed by prescribing appropriate boundary conditions over the symmetry planes. In this work however, a procedure is implemented for

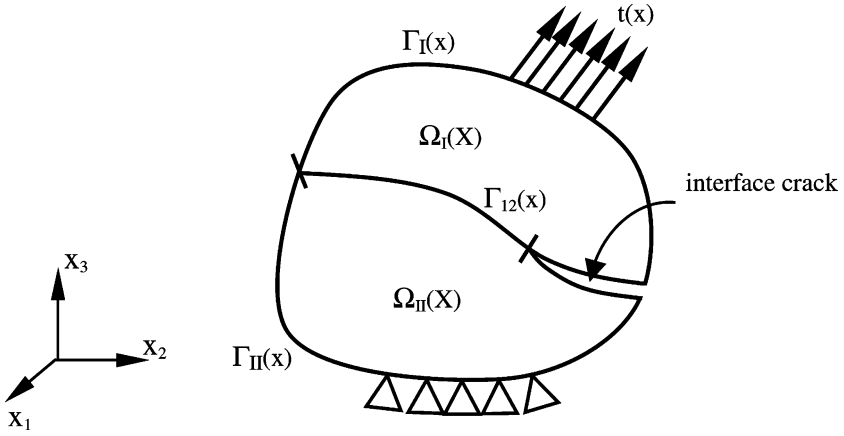

Figure 4. Schematic representation of the multidomain technique for a nonhomogeneous body.

modelling symmetric domains subjected either to symmetric or antisymmetric loadings which does not require neither the discretization nor the prescription of boundary conditions over the symmetry planes. This procedure redounds in both computer memory savings and numerical efficiency for the BEM implementation. Moreover, since loadings acting on a symmetric domain can always be decomposed into symmetric and antisymmetric parts, a single BEM discretization can be used to handle arbitrary loadings. Due to space restrictions the details of the implementation cannot be given here. For a comprehensive description of the procedure the reader is referred to the work by Kaijevic and Saigal (1995).

4.2. Displacement derivatives, stresses and strains

4.2.1. *Internal points*

As has been stated in Section 3, the computation of the J-integral and the application of the M_1-integral methodology requires the stress and displacement derivative fields σ^*_{ij} and $u^*_{j,k}$ to be known within the integration volume V. Although these quantities must be expressed in the local crack-front coordinate system x^*, in this work, and for the sake of simplicity, they will be first computed in the global system x and later transformed to the local system x^*. Bearing this in mind, and in order to integrate the computation of the fracture parameters into the BEM formulation, derivatives of the displacements at internal points X' are obtained from their boundary integral representations. The integral equation for the displacement derivatives results from the analytical differentiation of the well-known displacement boundary integral equation for a point X' located in the model domain (Brebbia et al., 1984):

$$u_{i,\mathrm{m}}(X') = \int_\Gamma U^*_{ij,\mathrm{m}}(X', x)\, t(x)\, \mathrm{d}\Gamma(x) - \int_\Gamma T^*_{ij,\mathrm{m}}(X', x)\, u(x)\, \mathrm{d}\Gamma(x), \tag{18}$$

where the terms $U^*_{ij,\mathrm{m}}$ and $T^*_{ij,\mathrm{m}}$ are the derivatives of the fundamental displacement U^*_{ij}, and traction T^*_{ij} solutions, and the boundary Γ corresponds to that of the zone where the point X' lies on.

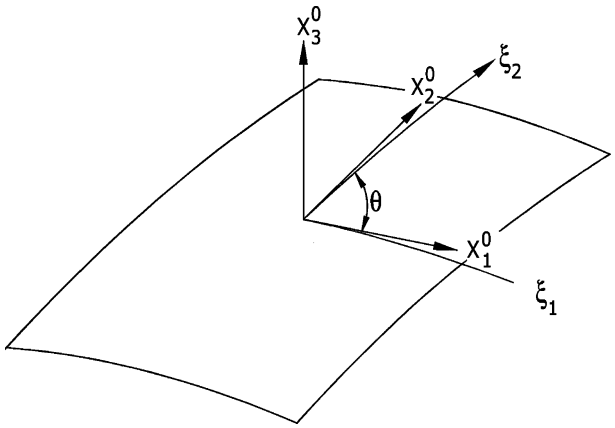

Figure 5. Local Cartesian system for boundary stress calculation.

Once the displacement derivatives $u_{i,\mathrm{m}}$ are known, stresses σ_{ij} and strains ε_{ij} can be computed using the basic continuum mechanics relationships:

$$\varepsilon_{ij} = \tfrac{1}{2}\left(u_{i,j} + u_{j,i}\right), \tag{19}$$

$$\sigma_{ij} = 2\mu\varepsilon_{ij} + \frac{2\mu\nu}{1-2\nu}\varepsilon_{kk}\delta_{ij}. \tag{20}$$

4.2.2. *Boundary points*

Displacement partial derivatives $u_{i,\mathrm{m}}$ at boundary nodes could be obtained from Equation (18), by taking the limit as point X' moves to the boundary, i.e. $X' \to x'$. However, this procedure is computationally expensive because of the occurrence of hypersingular integrands. In order to avoid this difficulty, stresses and strains, as well as the displacements on the model surface are evaluated in this work from the boundary displacements and tractions, following a procedure similar to that used in FEM computations. Consider with this purpose a local Cartesian system, (x_1^0, x_2^0, x_3^0) such that x_3^0 is the unit vector in the normal direction to the boundary element (see Figure 5). If u_j^0, ε_{ij}^0, σ_{ij}^0 and t_j^0 are the displacements, strains, stress and tractions in the local system, stress components in the normal direction can be written as:

$$\sigma_{i3}^0 = t_i^0, \quad i = 1, 2, 3. \tag{21}$$

The remaining stress tensor components, σ_{11}^0, σ_{12}^0 and σ_{22}^0 can be expressed in terms of t_3^0 and the tangential strain tensor components ε_{11}^0, ε_{12}^0 and ε_{22}^0, by eliminating ε_{33}^0 from the general expression of Hooke's law. Thus,

$$\sigma_{11}^0 = \frac{1}{1-\nu}\left[\nu t_3^0 + 2\mu\left(\varepsilon_{11}^0 + \nu\varepsilon_{22}^0\right)\right], \tag{22a}$$

$$\sigma_{22}^0 = \frac{1}{1-\nu}\left[\nu t_3^0 + 2\mu\left(\varepsilon_{22}^0 + \nu\varepsilon_{11}^0\right)\right], \tag{22b}$$

$$\sigma_{12}^0 = 2\mu\varepsilon_{12}^0. \tag{22c}$$

Strain components ε_{ij}^0 can be found using Equation (19), now applied in the local coordinate system. It is worth nothing that displacement derivatives in Equation (19) are initially evaluated in the intrinsic element directions (ξ_1, ξ_2), since as it usual in BEM, boundary displacements are given in terms of the piecewise parametric representation (shape functions) of intrinsic coordinates:

$$u_i(\xi_1, \xi_2) = \sum_{n=1}^{N} \Phi^n(\xi_1, \xi_2)\, u_i^n, \tag{23}$$

where Φ^n are the shape functions, u_i^n are the nodal values of the displacements, and N is the number of element nodes. From (23) it follows

$$\frac{\partial u_i}{\partial \xi_j} = \sum_{n=1}^{N} \frac{\partial \Phi^n}{\partial \xi_j} u_i^n. \tag{24}$$

Finally, the derivatives of the displacements in the global system are computed. Using chain differentiation, derivatives of the displacements in the global system, $u_{i,\mathrm{m}}$, can be related to the derivatives of the displacements in the intrinsic boundary element directions, $\partial u_i / \partial \xi_j$, as follows:

$$\frac{\partial u_i}{\partial \xi_j} = \frac{\partial u_i}{\partial x_\mathrm{m}} \frac{\partial x_\mathrm{m}}{\partial \xi_j}, \tag{25}$$

where $\partial x_m / \partial \xi_j$ is the Jacobian matrix of the transformation. The nine components of the displacement derivatives $u_{i,\mathrm{m}}$ can be retrieved by solving for each case a system of equations constructed using expressions (25). For further details the reader is referred to the works by Cisilino (2000) or Cisilino et al. (1998).

4.3. Implementation

As has been stated in Section 2, expressions (11) and (17) allow the computation of J-integral and the mixed-mode stress intensity factors at any position η on the crack front. In each case, the evaluation of a volume integral within a domain enclosing a segment of the crack front L_c is required. A natural choice here is to make η coincident with the element nodes on the crack front, while L_c is taken as the element or element sides at which points η lies (see Figure 6). The portion of the model domain in which the volume integrals are evaluated is discretized using 27-noded isoparametric (brick) cells, over which stresses, strains and displacements derivatives are approximated by products of the cell shape functions Ψ^i and the nodal values of σ_{ij}, ε_{ij} and $u_{i,j}$. Nodal values of these variables are computed following the procedures introduced in Sections 4.2.1 and 4.2.2, depending on whether the node is internal or lies on the model boundary. Volume discretization is designed to have web-style geometry around the crack front, while the integration volumes are taken to coincide with the different rings of cells. This is illustrated in Figure 7, where the frontal face of the model has been partially removed to show the crack and the integration domains.

As depicted in Figure 6, three different cases need to be considered, depending on whether the node of interest M is in the middle of an element side (mid-node), it is shared by two elements (corner node), or it is located coincident with the external

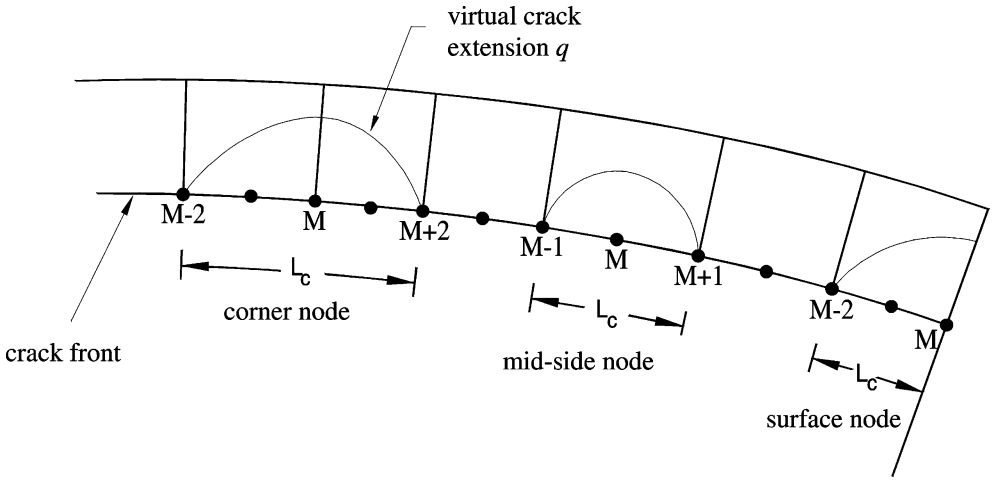

Figure 6. Schematic representation of the volume cells in the crack front region illustrating the virtual crack extensions for a corner node, a mid-node and a surface node.

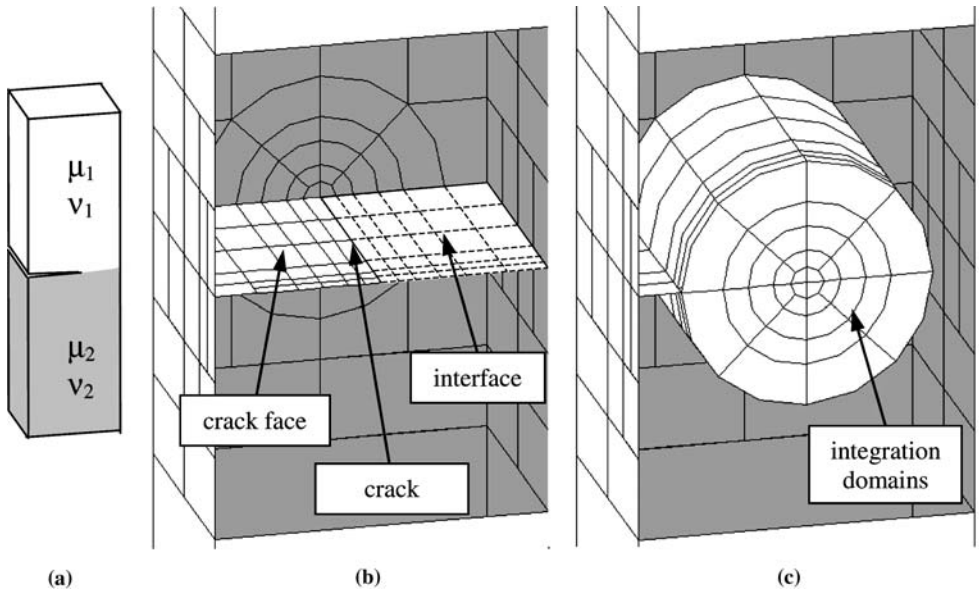

Figure 7. (a) Problem geometry, (b) Boundary Element discretization, (c) Integration domains.

surface (surface node). If the node M is a mid-node or surface node, L_c (the segment of the crack front over which the M_1-integral is computed) spans over one element, connecting nodes $M-1$, M, and $M+1$ and nodes $M-2$, $M-1$ and M, respectively. On the other hand, if M is a corner node, L_c spans over two elements, connecting nodes from $M-2$ to $M+2$.

The auxiliary function q was introduced in Section 3.1 in order to model the virtual crack front advance. Since the virtual crack advance can adopt any arbitrary shape, the only requirement for function q is to be sufficiently smooth within the integration volume V as the evaluation of the EDI requires of its differentiation (Moran and Shih, 1987). In this work q is defined to vary quadratically

in the directions tangential and normal to the crack front. Within this approach, and considering that the evaluation point η is at the middle of the crack front segment L_c, and r_0 is the radius of the integration domain, the function q is written as:

$$q(x^*) = \left| 1 - \left(\frac{x_3^*}{L_C/2} \right)^2 \right| \cdot \left[1 - \left(\frac{r}{r_0} \right)^2 \right], \tag{26}$$

where r is the distance from the crack front in the $x_1^* - x_2^*$ plane as depicted in Figure 2.

Although Moran and Shih (1987) have shown that for the EDI the computed value of J is insensitive to the selection of the q function, it has been found that the shape of the q function is relevant for the accuracy of the computations. Note that in contrast the path independent integrals, the EDI requires of the computation of quantities at crack front vicinity to calculate the domain integral. It is well known that accuracy of computed quantities at these points is lower than at those far from the crack front. The key feature for the excellent performance of the EDI under these circumstances is the behaviour of the auxiliary function q in the crack tip vicinity. Note that for the definition of q given in Equation (26), the gradient $q_{,i}$ tends to zero as r tends to zero (i.e. in the vicinity of the crack front), resulting that the contribution to J of the crack front fields is not significant (see Equation 10). As a consequence, the zone of the integration domain with the lowest accuracy in the results has a marginal contribution to the value of J. This fact also allows avoiding the use of quarter point or special crack tip elements to enhance the accuracy of the results in this zone. The bi-quadratic definition of q has been employed with excellent results in the computation of EDI for cracks in homogeneous materials in a previous work by one of the authors of this paper (Cisilino et al., 1998). Further details and discussion on the selection of the function q can be found in a recent work by the authors of this paper (Cisilino et al., 2004).

Function q is specified at all nodes within the integration volumes. Consistent with the isoparametric formulation, these q-values are given by:

$$q = \sum_{i=1}^{27} \Psi^i Q^i, \tag{27}$$

where Ψ^i are the shape functions defined within each volume cell and Q^i are the nodal values for the ith node. From the definition of q (see Equation (9)), $Q^i = 0$ if the ith node is on S_0, while for nodes inside V, Q^i are given by interpolating between the nodal values on L_c and S_0. Following standard manipulations:

$$q_{,j} = \sum_{i=1}^{27} \sum_{k=1}^{3} \frac{\partial \Psi^i}{\partial \zeta_k} \frac{\partial \zeta_k}{\partial x_i} Q^i, \tag{28}$$

where ζ_k are the coordinates in the cell isoparametric space and $\partial x_k / \partial \xi_j$ is the Jacobian matrix of the transformation.

If Gaussian integration is used, the discretized forms for the J-integral in Equation (10), and the M_1-integral in Equation (16) are given by:

$$\bar{I} = \sum_{\text{cells in } V} \sum_{p=1}^{m} \left\{ \left(\sigma_{ij}^* u_{j,k}^* - \sigma_{ij}^* \varepsilon_{ij}^* \delta_{ki} \right) q_{,i} \det \left(\frac{\partial x_j}{\partial \zeta_k} \right) \right\}_{\mathrm{p}} w_{\mathrm{p}} \tag{29}$$

and

$$M_1 = \sum_{\text{cells in } V} \sum_{p=1}^{m} \left\{ \left(\sigma_{ij}^{*(1)} u_{j,k}^{*(2)} + \sigma_{ij}^{*(2)} u_{j,k}^{*(1)} - \sigma_{ij}^{*(1)} \varepsilon_{ij}^{*(2)} \delta_{ki} \right) q_{,i} \det \left(\frac{\partial x_j}{\partial \zeta_k} \right) \right\}_{\mathrm{p}} w_{\mathrm{p}}, \tag{30}$$

respectively, where m is the number of Gaussian points per cell, and w_{p} are their weighting factors.

5. Examples

In this section the accuracy of BEM formulation and J-integral and stress intensity factor computations are assessed by considering a number of examples. The first examples have two-dimensional characteristics or deal with homogeneous materials (namely the embedded circular crack in a cylindrical bar and the panel with a centre slant crack) in order to allow comparisons with results from the bibliography. Finally, an example with three-dimensional characteristics (a thick centre-cracked bimaterial panel) is presented and the results discussed.

5.1. An external circumferential crack in a cylindrical bar

The first example is depicted in Figure 8(a), and it consists on an external circumferential crack in a cylindrical bar subjected to remote tension σ and torsion T. The material of the bar is homogenous, and thus, the traction on torsion load cases result in pure Mode-I and Mode-III fracture modes, respectively. The radius of the bar is $b = 5a$ and its height $h = 24a$, where a is the crack depth. Due to the symmetry in the model geometry, only one quarter of the problem is considered for the analysis of both load cases. The model is discretized using two zones as illustrated in Figure 8(b), and symmetrical and skew-symmetrical boundary conditions are applied implicitly for the tension and torsion load cases respectively (note the absence of discretization on the symmetry planes). A total of 96 elements and 453 nodes are employed in the model discretization. Four rings of cells with radii $r/a = 0.25, 0.5, 0.75$ and 1 are accommodated around the crack front for K computations. Integration domains are constructed using 108 cells.

Figure 8(c) and (d) illustrate the deformed configuration for the tension and torsion load cases, respectively. Computed stress intensity factors for the tension load case are reported in Table 1 at two positions on the crack front: for a point located coincident with the symmetry plane, $\theta/(\pi/2) = 0$, and for a point at the interior of the discretized portion of the model, $\theta/(\pi/2) = 0.5$. Results are normalized with respect to $\sigma\sqrt{\pi a}$ and compared with that reported by Tada et al. (2000). Computed values show to be almost independent with the integration volume, and constant

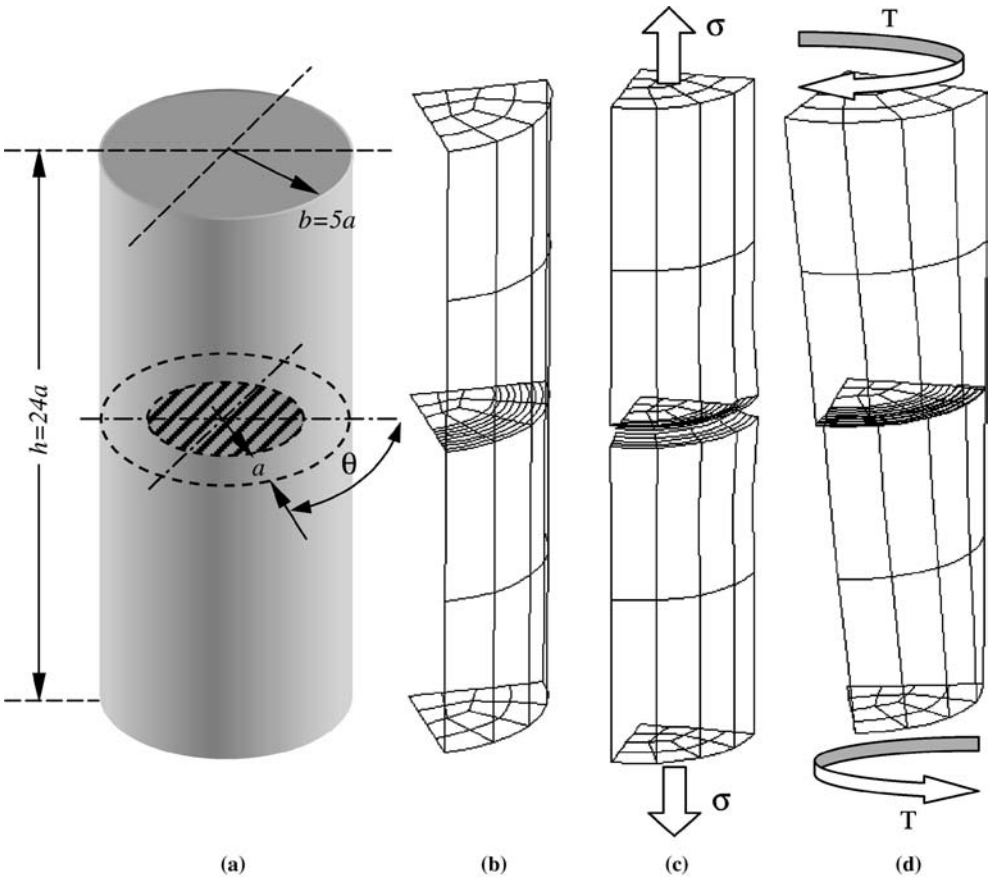

Figure 8. Embedded circular crack in a cylindrical bar, (a) geometry and dimensions, (b) model discretization, (c) deformed mesh for the traction load case, (d) deformed mesh for the torsion load case.

Table 1. Normalized K_I results for the external circumferential crack in a cylindrical bar under tension.

$\theta / \frac{\pi}{2}$	*r/a*				Average	Tada et al. (2000)	Δ[%]
	0.25	0.50	0.75	1.00			
0.00	1.177	1.183	1.193	1.197	1.188	1.256	−5.41
0.50	1.180	1.185	1.192	1.197	1.189	1.256	−5.33

along the crack front. Their deviation from the reference value is around 5%, which is considered adequate enough for the mesh used.

Results for the torsion load case are presented in Table 2, and normalized with respect to $\sigma\sqrt{\pi a}$. In this case the deviation from the reference value is less than 3%. On the other hand, the smallest integration volumes ($r/a = 0.25$) do not allow obtaining accurate results and they are excluded from the analysis.

Table 2. Normalized K_{III} results for the external circumferential crack in a cylindrical bar under tension.

$\theta \Big/ \frac{\pi}{2}$	r/a				Average*	Tada et al. (2000)	Δ[%]
	0.25	0.50	0.75	1.00			
0.00	0.278	0.321	0.322	0.324	0.322	0.322	−2.91
0.50	0.278	0.322	0.322	0.325	0.323	0.332	−2.71

*Result for $r/a = 0.25$ are excluded

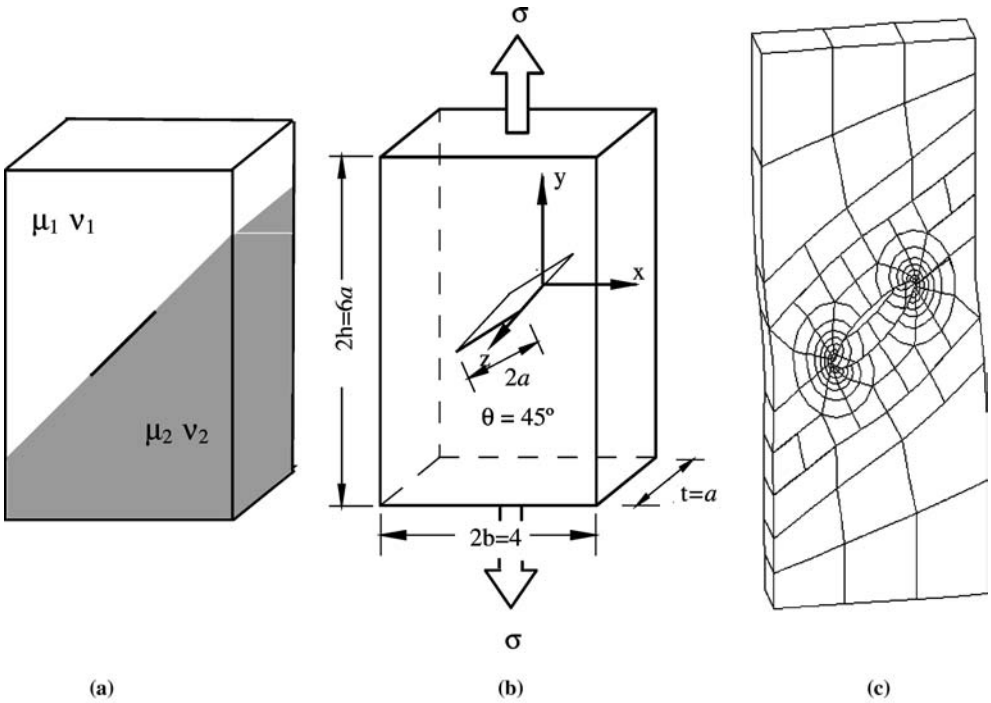

Figure 9. (a) Schematic representation of the panel with a center slant crack, (b) Model dimensions, (c) Boundary element mesh (deformed).

5.2. Tension panel with a slant interface crack

This second example deals with a crack under remote mixed load conditions. It consists on a thin panel with a slant interface crack rotated $\theta = 45^\circ$ with respect to the horizontal, and subjected to a uniaxial remote tension σ. A schematic representation with the problem geometry and dimensions is depicted in Figure 9 together with a view of the deformed mesh. Specimen dimensions are $a = 2.5\,\text{mm}$, $b = 2a$, $h = 3b$ and $t = a$. The model is divided into two zones and discretized using 842 nodes and 171 boundary elements. Normal displacements of the model lateral faces are restricted in order to simulate a plain strain condition and allow comparison with results from the bibliography. Twenty elements are used in the crack discretization. Only one element is placed in the direction of the thickness of the model. Six rings of cells with radii $r/a = 0.167$, 0.33, 0.5, 0.666, 0.833 and 1 are accommodated around the crack

Table 3. Normalized K_I results for the slant crack in a homogeneous panel.

Position	*r/a*				Average	Miyazaki et al. (1993)	Δ[%]
	0.250	0.333	0.4165	0.500			
Surface	0.431	0.431	0.431	0.431	0.431	0.433	−0.46
Mid-plane	0.430	0.430	0.430	0.431	0.430	0.433	−0.70

Table 4. Normalized K_{II} results for the slant crack in a homogeneous panel.

Position	*r/a*				Average	Miyazaki et al. (1993)	Δ[%]
	0.250	0.333	0.4165	0.500			
Surface	−0.378	−0.379	−0.380	−0.380	−0.379	−0.386	1.81
Mid-plane	−0.380	−0.382	−0.383	−0.383	−0.382	−0.386	1.04

Table 5. Normalized K_I results for the slant crack in a bimaterial panel.

Position	*r/a*				Average	Miyazaki et al. (1993)	Δ[%]
	0.250	0.333	0.4165	0.500			
Surface	0.367	0.367	0.368	0.368	0.368	0.368	0.22
Mid-plane	0.365	0.365	0.365	0.365	0.365	0.368	0.96

Table 6. Normalized K_{II} results for the slant crack in a bimaterial panel.

Position	*r/a*				Average	Miyazaki et al. (1993)	Δ[%]
	0.250	0.333	0.4165	0.500			
Surface	−0.466	−0.465	−0.464	−0.462	−0.464	−0.474	2.11
Mid-plane	−0.464	−0.465	−0.463	−0.462	−0.464	−0.474	2.11

front for J and K computations. With this purpose 44 cells are employed. Two sets of materials properties are considered. For the first analysis the plate is considered homogeneous, and thus, identical material properties are used for both zones. For the second analysis a set of dissimilar material properties is considered with $E_1/E_2 = 10$ and $\nu_1 = \nu_2 = 0.3$.

Computed stress intensity factors are presented in Tables 3 and 4 for the homogeneous example, while the results for the bimaterial case are reported in Tables 5 and 6. All values are normalized with respect to $\sigma\sqrt{\pi a}$ and compared to those reported by Miyazaki et al. (1993). Very good agreement is achieved between the obtained results and those from the reference.

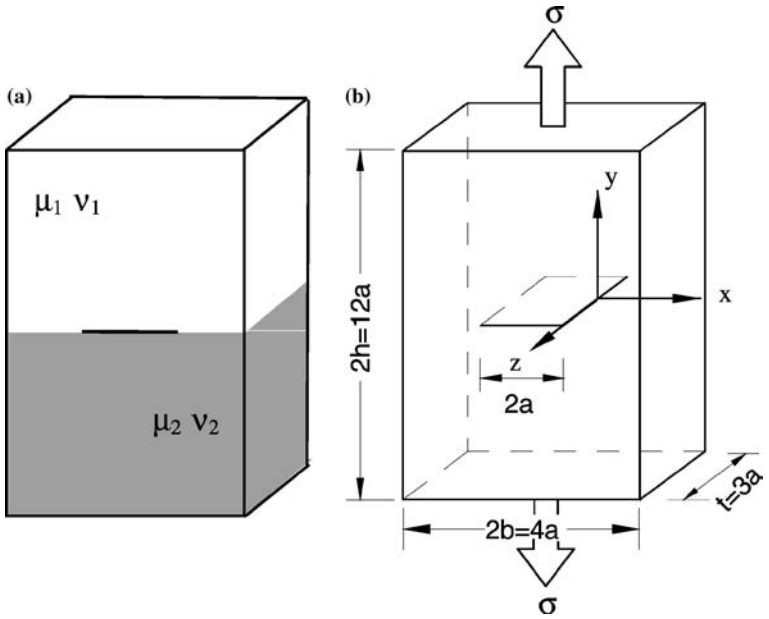

Figure 10. (a) Schematic representation of the thick tension plate with a centre interface crack, (b) Model dimensions.

5.3. Thick tension bimaterial plate with a centre interface crack

For the three-dimensional study a bimaterial plate containing a through crack on the interface is considered. A schematic representation of the problem geometry and dimensions are depicted in Figure 10. The example is analysed for seven sets of material properties. In first place the homogeneous case is considered in order to allow the comparison with results reported in the literature. The next five cases correspond to bimaterial plates with the following ratios of Young modulus: $E_1/E_2 = 3$, 10, 20, 40 and 80, and Poisson ratios $\nu_1 = 0.2$ and $\nu_2 = 0.4$ ($\mu_1/\mu_2 = 3.5$, 11.67, 23.33, 46.67, 93.33 for each case). The oscillatory behaviour in the asymptotic stress and deformation fields is given by the oscillatory parameter ($\varepsilon = 0$, 0.00548, 0.0355, 0.044, 0.0486 and 0.051 for each case), while the extent of the bimaterial mismatch can be measured by the Dundurs′ parameter ($\alpha = 0.448$, 0.795, 0.892, 0.944 and 0.972). Finally, a bimaterial plate composed by glass ($E_2 = 70.8\,\text{GPa}$, $\nu_2 = 0.22$) and epoxy ($E_1 = 2.79\,\text{GPa}$, $\nu_1 = 0.33$) with $\alpha = 0.919$, and $\varepsilon = 0.074$ is also analysed. Due to the symmetry of the problem, only one quarter of the problem is modelled. Model discretization consists of 296 elements and 1341 nodes. Mesh design is similar to that illustrated in Figure 7. Crack front element dimensions are graded towards the free surface, being the smallest equal to $t/64$. Six rings of cells with radii $r/a = 0.09$, 0.15, 0.225, 0.338, 0.5 and 0.75 are employed for J-integral and stress intensity factor computations. The number of cells used with this purpose is 312.

J-integral and stress intensity factor results for the bimaterial plates are plotted in Figure 11 and Figures 12–14, respectively. The origin of the normalized coordinate z/t corresponds to the specimen mid-plane. Results are normalized with respect to the J-integral and stress intensity factor values for a crack in a infinite bimaterial

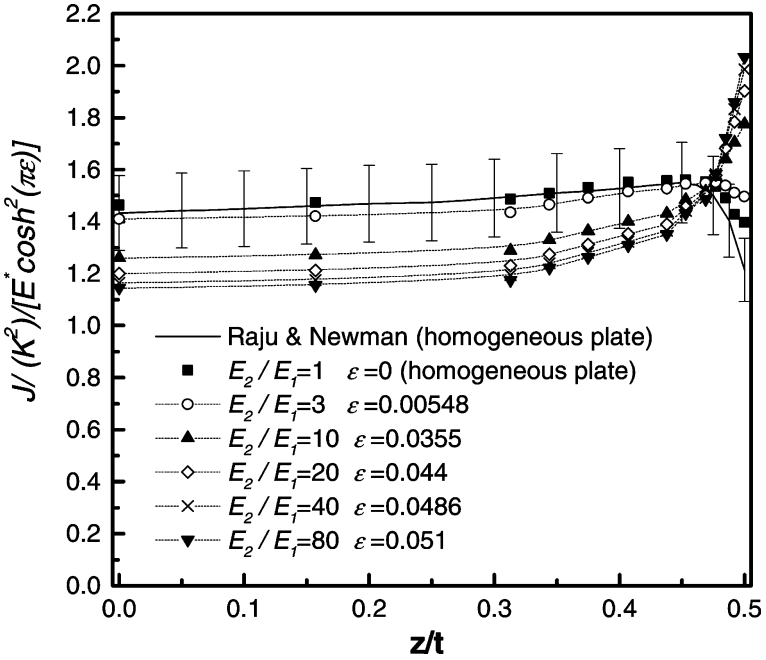

Figure 11. *J*-integral along the crack front for various bimaterial combinations. Error bars indicate the accuracy of the solution for the homogeneous plate by Raju and Newman (1977).

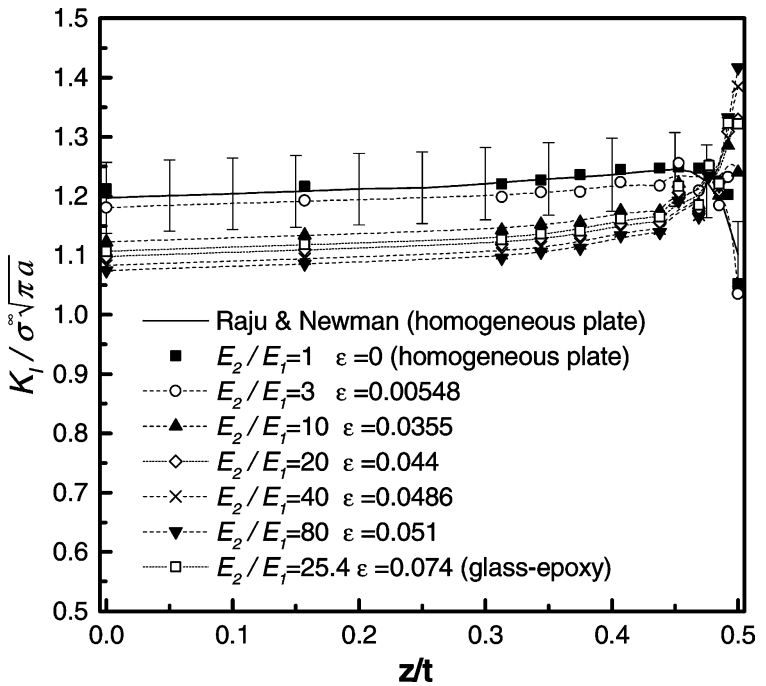

Figure 12. K_{I} along the crack front for various bimaterial combinations. Error bars indicate the accuracy of the solution for the homogeneous plate by Raju and Newman (1977).

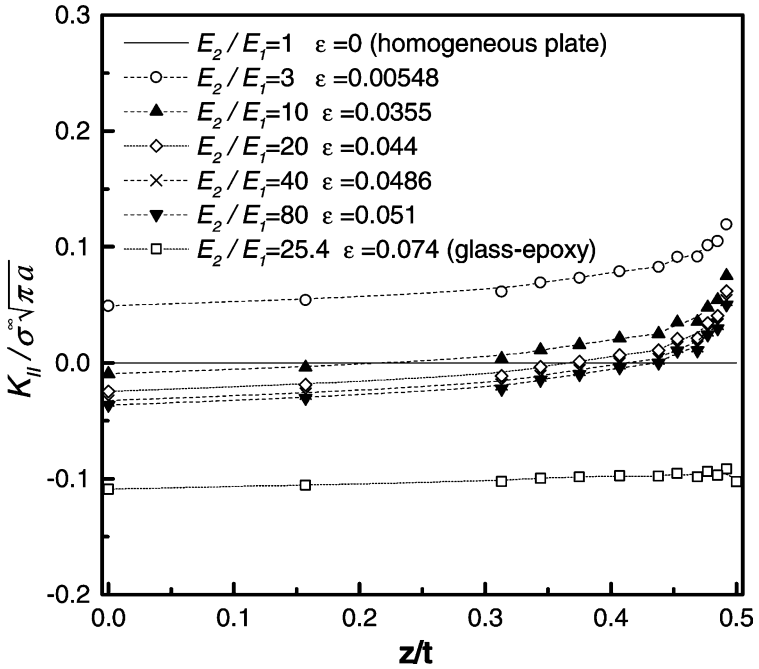

Figure 13. K_{II} along the crack front for various bimaterial combinations.

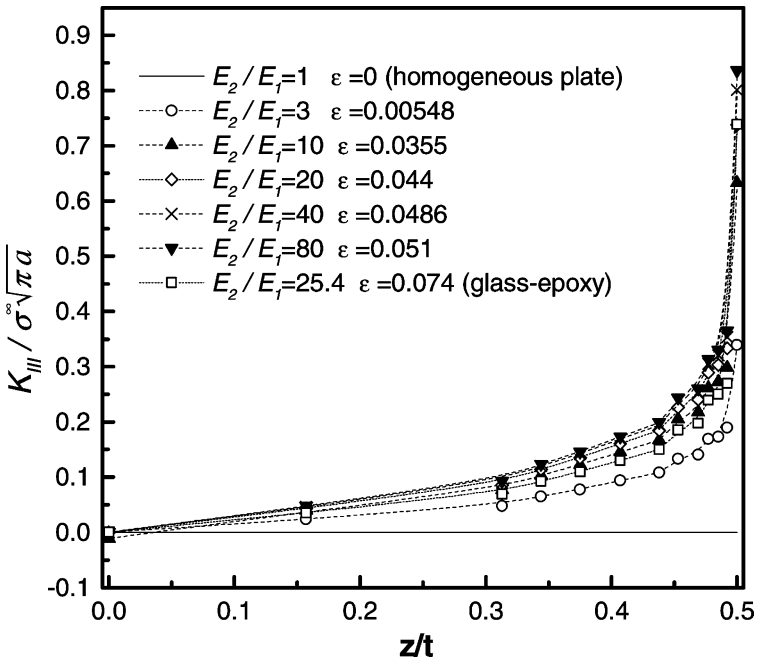

Figure 14. K_{III} along the crack front for various bimaterial combinations.

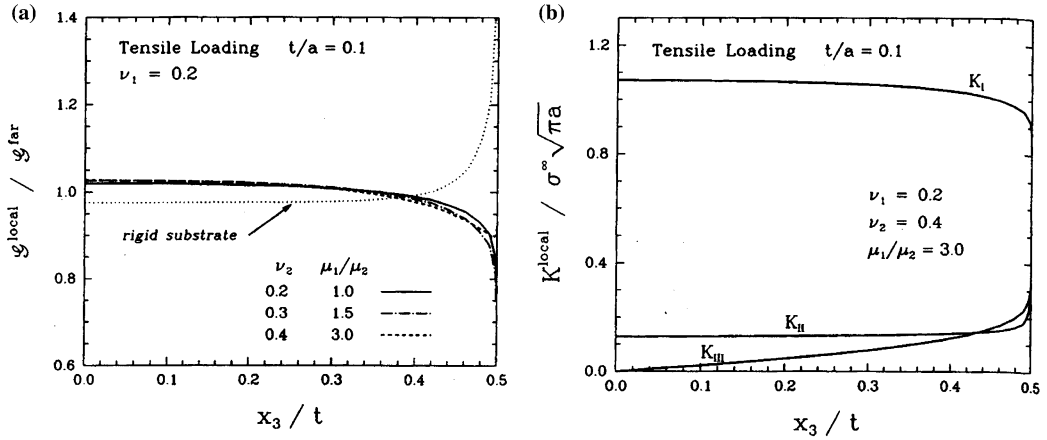

Figure 15. (a) Normalized energy release rate, and (b) stress intensity factor components along the crack front for the interface crack in a thin infinite plate with various bimaterial combinations (from Nakamura and Parks, 1989).

plate, $J_o = (K)^2/[E^* \cosh^2(\pi\varepsilon)]$ and $K = \sigma^\infty[(1+4\varepsilon^2)\pi a]^{1/2}$, where E^* is the effective elastic modulus defined in Equation (6). Also included in the Figures 11 and 12 are the reference values due to Raju and Newman (1977) for the homogeneous plate. Reference values were calculated using FEM with a reported accuracy of 5% for the stress intensity factors. Note that since the reference values for the *J*-integral are obtained from their stress intensity factor counterparts using Equation (5), their accuracy is reduced to around 10%. Accuracy of the reference values is indicated using the error bars.

Excellent agreement is found between the reported and computed results throughout the specimen thickness.The only exception are the points located very close to the free surface ($z/t = 0.5$), where the computed values are misleading due to the dominance of the corner singularity (Bazant and Estenssoro, 1979; Barsoum and Chen, 1991; Ghahremani and Shih, 1992). Note that with the exception of these points the deviation of the computed results from those of the reference is always smaller than the reported accuracy of the reference.

Results in Figure 11 allow seeing the dependence of the *J*-integral behaviour along the crack front with the material mismatch. Taking the homogeneous case as a reference value, the increment in the oscillatory index ε induces a reduction in the value of J in the zone close to the specimen mid-plane ($z/t = 0$), where a plain strain condition prevails. For the crack front positions close to the free surface ($z/t = 0.5$), the *J*-integral values present a strong dependence with the material mismatch. It can be observed that for low ε values, *J*-integral remains almost constant or decreases towards the free surface. On the other hand, high values of ε make the *J*-integral level to increase towards the free surface. This same general behaviour has been reported by Nakamura (1991), who studied an interface crack embedded in a thin infinite bimaterial plate ($2b = 2h = 60a, t = a/10$) using high-resolution FEM models. Nakamura's results (Nakamura, 1991) are reproduced in Figure 15, for two different situations. The first one corresponds to bimaterial combinations that although dissimilar, their oscillatory behaviour in the asymptotic stress field disappear as they

yield $\varepsilon = 0$. The second situation corresponds to the limiting case given by an elastic-rigid substrate model with a mismatch $\varepsilon = 0.1255$. It can be observed that while the J-integral values diminish towards the free surface for all the material combinations with $\varepsilon = 0$, for the elastic-rigid substrate case they increase. This behaviour is attributed to the much greater level of shearing condition affecting the crack tip-field. In the same sense, results by Nakamura and Parks (1989) have shown that the behaviour of energy release rate along the crack front is directly related to the amount of in-plane and antiplane shear in the crack front surrounding region. In a bimaterial plate, even in the absence of any remote loading, the antisymmetrical conditions are induced by the material mismatch along the interface.

Figures 12–14 show the variation of the stress intensity factor components along the crack front. Due to the relatively small bimaterial mismatch the tensile force is dominant and values of K_{II} and K_{III} are relatively small when compared to K_I. Near the free surface, the amplitudes of both antisymmetrical modes increase, while K_I shows a similar behaviour to that exhibited by J-integral. Similar results are also reported by Nakamura (1991) for the case of thin plates with $\varepsilon = 0$ (see Figure 17). The obtained results allow concluding that although K_I exhibit a general behaviour similar to that of J-integral, K_I level is dominated by the relative stiffness E_2/E_1 instead of the oscillatory parameter ε. As can be seen in Figure 12, the increment of E_2/E_1 is accompanied by a decrement in the K_I level at the interior of the specimen. In this context it is worth to note the response of the glass/epoxy bimaterial, which although having the largest ε, its relative stiffness $E_2/E_1 = 25$ makes the K_I results to behave very close to those obtained for $E_2/E_1 = 20$. On the other hand, the oscillatory index governs the behaviour of K_{II} (see Figure 13). In this case, small values of ε induce the highest values of K_{II}, which monotonically diminish with the increment of ε. Finally K_{III} behaves almost independently of both ε and E_2/E_1, as can be seen from Figure 14.

6. Conclusions

A boundary element methodology for the three-dimensional analysis of bimaterial interface cracks has been presented in this paper. The interface crack analysis is addressed using a multidomain BEM formulation in order to account for the different material properties at both sides of the crack. Fracture mechanics parameters, namely J-integral and stress intensity factors, are computed along the crack front using the Energy Domain Integral and the Interaction Integral methodologies. These are implemented as a post-processing technique, and so it can be applied to the results from a particular model at a later stage. The implementation takes advantage of the efficiency of the boundary integral equation to directly obtain the required displacement derivatives, stress and strain fields from their boundary integral representations. The efficiency and accuracy of the proposed implementation has been addressed by analysing a number of examples, and their results compared with those available in the bibliography.

The devised numerical tool is employed to analyze the case of a thick bimaterial plate with a centre interface crack under tension. Obtained results allow studying the dependence of the J-integral and stress intensity factor behaviour with the material mismatch. It is observed that for the crack front positions close to the free surface,

the J-integral values present a strong dependence with the material mismatch. For low values of the oscillatory index ε, J-integral remains almost constant or decreases towards the free surface. On the other hand, high values of ε make the J-integral level to increase towards the free surface. K_{I} exhibits a general behaviour similar to that of J-integral, but its behaviour is dominated by the relative stiffness E_2/E_1 instead of the oscillatory index ε. The oscillatory index governs the behaviour of K_{II}, while K_{III} behaves almost independently of both ε and E_2/E_1.

Acknowledgements

This work was financed by grant PICT 12-12528 of Agencia Nacional de Promoción Científica de la República Argentina and the University of Mar del Plata.

Appendix A

In this Appendix the auxiliary asymptotic solutions of stress σ_{ij} and displacements u_i, for the extraction of the mode I and II stress intensity factors are given. The expressions are due to Williams (1959), and they are referred to the local $x_1 - x_2$ plane (see Figure 2).

$$(\sigma_{11})_j = \frac{K_{\mathrm{I}}}{2\sqrt{2\pi r}}\left[\omega_j f_{11}^{\mathrm{I}} - \frac{1}{\omega_j}\cos(\theta-\bar{\Theta})\right] - \frac{K_{\mathrm{II}}}{2\sqrt{2\pi r}}\left[\omega_j f_{11}^{\mathrm{II}} + \frac{1}{\omega_j}\sin(\theta-\bar{\Theta})\right], \quad \text{(A.1)}$$

$$(\sigma_{22})_j = \frac{K_{\mathrm{I}}}{2\sqrt{2\pi r}}\left[\omega_j f_{22}^{\mathrm{I}} - \frac{1}{\omega_j}\cos(\theta-\bar{\Theta})\right] - \frac{K_{\mathrm{II}}}{2\sqrt{2\pi r}}\left[\omega_j f_{22}^{\mathrm{II}} - \frac{1}{\omega_j}\sin(\theta-\bar{\Theta})\right], \quad \text{(A.2)}$$

$$(\sigma_{12})_j = \frac{K_{\mathrm{I}}}{2\sqrt{2\pi r}}\left[\omega_j f_{12}^{\mathrm{I}} - \frac{1}{\omega_j}\sin(\theta-\bar{\Theta})\right] - \frac{K_{\mathrm{II}}}{2\sqrt{2\pi r}}\left[\omega_j f_{12}^{\mathrm{II}} - \frac{1}{\omega_j}\cos(\theta-\bar{\Theta})\right], \quad \text{(A.3)}$$

$$(u_1)_j = \frac{K_{\mathrm{I}}\sqrt{2\pi r}}{4\pi\mu_j}\left[\kappa_j\omega_j h_{11} - \frac{1}{\omega_j}h_{12} + \omega_j h_{13}\right] + \frac{K_{\mathrm{II}}\sqrt{2\pi r}}{4\pi\mu_j}\left[\kappa_j\omega_j h_{21} - \frac{1}{\omega_j}h_{22} + \omega_j h_{23}\right], \quad \text{(A.4)}$$

$$(u_2)_j = \frac{K_{\mathrm{I}}\sqrt{2\pi r}}{4\pi\mu_j}\left[\kappa_j\omega_j h_{21} - \frac{1}{\omega_j}h_{22} - \omega_j h_{23}\right] + \frac{K_{\mathrm{II}}\sqrt{2\pi r}}{4\pi\mu_j}\left[-\kappa_j\omega_j h_{11} + \frac{1}{\omega_j}h_{12} + \omega_j h_{13}\right], \quad \text{(A.5)}$$

where

$$\alpha = \frac{1}{2\pi}\ln\left[\left(\frac{\kappa_1}{\mu_1} + \frac{1}{\mu_2}\right)\Big/\left(\frac{\kappa_2}{\mu_2} + \frac{1}{\mu_1}\right)\right] \quad \text{(A.6)}$$

$$\bar{\Theta} = \alpha\,\ln\left(\frac{r}{2a}\right) + \frac{\theta}{2}, \quad \text{(A.7)}$$

$$\kappa_j = 3 - 4\nu_j, \tag{A.8}$$

$$\omega_1 = e^{-\alpha(\pi-\theta)}, \tag{A.9}$$

$$\omega_2 = e^{\alpha(\pi+\theta)}, \tag{A.10}$$

$$f_{11}^{\mathrm{I}} = 3\cos\bar{\Theta} + 2\alpha\sin\theta\cos(\theta+\bar{\Theta}) - \sin\theta\sin(\theta+\bar{\Theta}), \tag{A.11}$$

$$f_{11}^{\mathrm{II}} = 3\sin\bar{\Theta} + 2\alpha\sin\theta\sin(\theta+\bar{\Theta}) + \sin\theta\cos(\theta+\bar{\Theta}), \tag{A.12}$$

$$f_{22}^{\mathrm{I}} = \cos\bar{\Theta} - 2\alpha\sin\theta\cos(\theta+\bar{\Theta}) + \sin\theta\sin(\theta+\bar{\Theta}), \tag{A.13}$$

$$f_{22}^{\mathrm{II}} = \sin\bar{\Theta} - 2\alpha\sin\theta\sin(\theta+\bar{\Theta}) - \sin\theta\cos(\theta+\bar{\Theta}), \tag{A.14}$$

$$f_{12}^{\mathrm{I}} = \sin\bar{\Theta} + 2\alpha\sin\theta\sin(\theta+\bar{\Theta}) + \sin\theta\cos(\theta+\bar{\Theta}), \tag{A.15}$$

$$f_{12}^{\mathrm{II}} = -\cos\bar{\Theta} - 2\alpha\theta\cos(\theta+\bar{\Theta}) + \sin\theta\sin(\theta+\bar{\Theta}), \tag{A.16}$$

$$h_{11} = \frac{1}{1+4\alpha^2}\left[\cos(\theta-\bar{\Theta}) - 2\alpha\sin(\theta-\bar{\Theta})\right], \tag{A.17}$$

$$h_{12} = \frac{1}{1+4\alpha^2}\left[\cos\bar{\Theta} + 2\alpha\sin\bar{\Theta}\right], \tag{A.18}$$

$$h_{13} = \sin\theta\sin\bar{\Theta}, \tag{A.19}$$

$$h_{21} = \frac{1}{1+4\alpha^2}\left[\sin(\theta-\bar{\Theta}) + 2\alpha\cos(\theta-\bar{\Theta})\right], \tag{A.20}$$

$$h_{22} = \frac{1}{1+4\alpha^2}\left[-\sin\bar{\Theta} + 2\alpha\cos\bar{\Theta}\right], \tag{A.21}$$

$$h_{23} = \sin\theta\cos\bar{\Theta}, \tag{A.22}$$

The difference between the properties of an interface crack under anti-plane strain and a mode III crack in an homogeneous medium is quite modest, as the displacement and stress fields at each side of the interface are the same to the mode III of separated homogeneous bodies. In this way

$$(\sigma_{13})_j = -\frac{K_{\mathrm{III}}}{\sqrt{2\pi r}}\sin\left(\frac{\theta}{2}\right), \tag{A.23}$$

$$(\sigma_{23})_j = -\frac{K_{\mathrm{III}}}{\sqrt{2\pi r}}\cos\left(\frac{\theta}{2}\right), \tag{A.24}$$

$$(u_3)_j = 2\frac{1+\nu_j}{E_j}\sqrt{\frac{2r}{\pi}}K_{\mathrm{III}}\sin\left(\frac{\theta}{2}\right). \tag{A.25}$$

References

Barsoum, R.S. and Chen, T-K. (1991). Three-dimensional surface singularity of an interface crack. *International Journal of Fracture* **50,** 221–237.

Bazant, Z.P. and Estenssoro, L.F. (1979). Surface singularity and crack propagation. *International Journal of Solids and Structures* **15,** 405–426.

Beer, G. (1993). An efficient numerical method for modelling initiation and propagation of cracks along material interfaces. *International Journal of Numerical Methods in Engineering* 3579–3594.

Brebbia, C.A., Telles, J.L.F. and Wrobel, L.C. (1984). Boundary Element Techniques. Springer Verlag, Berlin.

Carpenter, W.C., Read, D.T. and Dodds, R.H. (1986). Comparison of several path independent integrals including plasticity effects. *International Journal of Fracture* 303–323.

Chen, F.H.K. and Shield, R.T. (1977). Conservation laws in elasticity of the *J*-integral type. *Journal of Applied Mathematical Physics* (*ZAMP*), **28,** 1–22.

Cho, S.B., Lee, K.R., Coi, Y.S. and Yuuki, R. (1992). Determination of stress intensity factors and boundary element analysis for interface cracks in dissimilar anisotropic materials. *Engineering Fracture Mechanics* **43,** 603–614.

Cisilino, A.P. (2000). Linear and Nonlinear Crack Growth using Boundary Elements. Southampton, WIT Press, UK.

Cisilino, A.P. and Aliabadi, M.H. (1999). BEM implementation of the energy domain integral for the elastoplastic analysis of 3D fracture problems. *International Journal of Fracture* **96,** 229–245.

Cisilino, A.P., Aliabadi, M.H. and Otegui, J.L. (1998). Energy domain integral applied to solve center and double-edge crack problems in three-dimensions. *Theoretical and Applied Fracture Mechanics* **29,** 181–194.

Cisilino, A.P. and Ortiz, J.E. (2004). Boundary Element Analysis of Three-Dimensional Mixed-Mode Cracks via the Interaction Integral. *Computer Methods in Applied Mechanics and Engineering* **194**(9–11), 935–956.

Comninou, M. (1977). The interface crack. *ASME Journal of Applied Mechanics* **44,** 631–636.

de Paula, F.A. and Aliabadi, M.H. (1997). Boundary element analysis of interface cracks in dissimilar orthotropic materials using path independent contour integral. Boundary Elements XIX, Computational Mechanics Publications, Southampton, UK.

Dundurs, J. (1969). Edge-bonded dissimilar orthogonal elastic wedges under normal and shear loading. *ASME Journal of Applied Mechanics* **36,** 650–652.

Ghahremani, F. and Shih, C.F. (1992). Corner singularities of three-dimensional planar interface cracks, *Journal of Applied Mechanics* **59,** 61–68.

Gosz M., Dolbow, J. and Moran, B. (1988). Domain integral formulation for stress intensity factor computation along curved three-dimensional interface cracks. *International Journal of Solids and Structures* **35**(15), 1763–1783.

He W.J., Lin, D.S. and Ding, H.J. (1994). A boundary element for crack analysis at a bimaterial interface. *Engineering Fracture Mechanics* **49**(3), 405–410.

Hellen, T.K.(1975). On the method of virtual crack extensions. *International Journal of Numerical Methods in Engineering* 187–207.

Hutchinson, J.W., Mear, W., and Rice, J.R. (1987). Crack paralleling and interface between dissimilar materials. *ASME Journal of Applied Mechanics* **54,** 828–832.

Kaijevic, I. and Saigal, S. (1995). Analysis of symmetric domains in advanced applications with the boundary element method. *International Journal of Numerical Methods in Engineering* **38,** 2373–2388.

Kwon, Y.W. and Dutton, R. (1991). Boundary element analysis of cracks normal to bimaterial interfaces. *Engineering Fracture. Mechanics* **40,** 487–491.

Lui, Y.J. and Xu, N. (2000). Modelling of interface cracks in fibre-reinforced composites with the presence of interphases using the boundary element method. *Mechanics of Materials* **32,** 769–783.

Mao, R. and Sun, G. (1995). A study of the interaction between matrix crack and matrix-fibre interface. *Engineering Fracture Mechanics* **51**(3), 469–477.

Miyazaki, N., Ikeda, T., Soda, T. and Munakata, T. (1993). Stress intensity factor analysis of interface crack using boundary element method – Application of contour-integral method. *Engineering Fracture Mechanics* **45**(5), 599–610.

Moran, B. and Shih, C.F. (1987). A general treatment of crack tip contour integrals. *International Journal of Fracture* 295–310.

Nagashima, T., Omoto, Y. and Tani, S. (2003). Stress intensity factor analysis of interface cracks using X-FEM. *International Journal of Numerical Methods in Engineering* **56,** 1151–1173.

Nakamura, T. (1991). Three-dimensional stress fields of elastic interface cracks. *ASME Journal of Applied Mechanics* **58,** 939–946.

Nakamura, T. and Parks, D.M. (1989). Anti-symmetrical 3D stress field near the crack front of a thin elastic plate. *International Journal of Solids and Structures* **25,** 1411–1416.

Natha, R. and Moran, B. (1993). Domain integrals for axisymmetric interface crack problems. *International Journal of Solids and Structures* **30(**15), 2027–2040.

Nikishkov, G.P. and Atluri, S.N. (1987). Calculation of fracture mechanics parameters for an arbitrary three-dimensional crack by the equivalent domain integral method. *International Journal of Numerical Methods in Engineering* 1801–1821.

París, F., del Caño, J.C. and Varna, J. (1996). The fibre-matrix interface crack – A numerical analysis using boundary elements. *International Journal of Fracture* **82,** 11–29.

Parks, D.M. (1974). A stiffness derivative finite element technique for determination of elastic crack tip stress intensity factors. *International Journal of Fracture* 487–502.

Raju, I.S. and Newman, J.C. (1977). Three-dimensional finite element analysis of finite-thickness fracture mechanics, Technical Report NASA TN D-8414.

Raveendra, S.T. and Banerjee, P.K. (1991). Computation of stress intensity factors for interfacial cracks. *Engineering Fracture Mechanics* **40**(1), 89–103.

Rice, J.R. (1968). A path independent integral and the approximate analysis of strain concentration by notches and cracks. *ASME Journal of Applied Mechanics* 379–386.

Rice, J.R. (1988). Elastic fracture mechanics concepts for interfacial cracks. *ASME Journal of Applied Mechanics* **55,** 98–103.

Rice, J.R., Suo, Z. and Wang, J.S. (1990). Mechanics and thermodynamics of brittle interfacial failure in bimaterial systems, Metal-Ceramics Interfaces, (edited by M.Ruhle et al.), Pergamon Press, Oxford, New york, pp. 269–294.

Saliva, R., Vènere, M.J., Padra, C., Taroco, E. and Feijoo, R.A. (2000). Shape sensitivity analysis and energy release rate of planar cracks embedded in three-dimensional bodies. *Computer Methods in Applied Mechanics and Engineering* **188,** 649–664.

Selcuk, S., Hurd, D.S., Crouch, S.L. and Gerberich, W.W. (1994). Prediction of interfacial crack path: a direct boundary integral approach and experimental study. *International Journal of Fracture* **67,** 1–20.

Sladek, J. and Sladek, V. (1997). Evaluation of the T-stress for interface cracks by the boundary element method. *Engineering Fracture Mechanics* **56**(6), 813–825.

Tada, H., Paris, P. and Irwin, G.R. (2000). The stress Analysis of Crack Handbook. ASME Press, Newyork.

Tan, C.L. and Gao, Y.L. (1990). Treatment of bimaterial interface crack problems using the boundary element method. *Engineering Fracture Mechanics* **36,** 919–932.

Varna, J., París, F. and del Caño, J.C. (1997). The effect of crack-face contact on fibre/matrix debonding in transverse tensile loading. *Composites Science and Technology* **57,** 523–532.

Wen, P.H. and Aliabadi, M.H. (1999). Evaluation of the stress intensity factor for a three-dimensional interfacial crack by the boundary element method. *Journal of Strain Analysis* **34**(3), 209–215.

Williams, M.L. (1959). The stress around a fault or crack in dissimilar media. *Bulletin of the Seismological Society of America* **49**, 199–204.

Yuuki, R., and Cho, S.B. (1989). Efficient boundary element analysis of stress intensity factors for interface cracks in dissimilar materials. *Engineering Fracture Mechanics* **34,** 179–188.

Yuuki, R. and Xu, J-Q. (1994). Boundary element analysis of dissimilar materials and interface crack. *Computational Mechanics* **14,** 116–127.